An investigation of the plane-concave Fabry Perot cavity

THESIS

submitted in partial fulfillment of the
requirements for the degree of

MASTER OF SCIENCE
in
PHYSICS

Author :	Jeroen van Doorn
Student ID :	s1267930
Supervisor :	Dr. Wolfgang Löffler
2^{nd} corrector :	Dr. Peter Gast

Leiden, The Netherlands, October 30, 2019

An investigation of the plane-concave Fabry Perot cavity

Jeroen van Doorn

Huygens-Kamerlingh Onnes Laboratory, Leiden University
P.O. Box 9500, 2300 RA Leiden, The Netherlands

October 30, 2019

Abstract

Fabry-Perot cavities are generally used in cavity QED. Due to technical restraints it is prudent to evaluate the ability to create open micro cavities in the weakly coupled regime. We have focussed on building the foundation for the weakly coupled cavity by charactarizing a macroscopic cavity in detail. We analyse the cavity effects, for the fundamental and higher order modes. Using the primary mode of a plane-curved mirror cavity we found the Free Spectral Range in multiple ways, and looking at transmission spectra as a function of wavelenght we found a spectrum of transmission peaks with a predictable mode ordering. Thus the cavity was found to be consistent with theory. The system has been improved upon by presenting an extensive model for modematching. The model is capable of determining the coupling efficiency after introducing a lens with any focal length and possible position. With the model we were able to find a setup configurations with near unity coupling efficiency to the fundamental mode of the cavity.

Contents

Chapter 1

Introduction

Optical cavities are devices build to enhance the electromagnetic field. Comparable with a tuning fork for acoustical systems, the optical cavity allows for resonance at specific frequencies [1]. Starting from the past decade a shift has occurred in the creation of optical cavities from building cavities not as macroscopic devices, towards shrinking them down to the microscopic regime to generate additional quantum effects [2]. This shift has been crucial in the development of several theories, having spawned an entire field of its own: cavity Quantum Electro Dynamics QED.
Using the cavity to trap light and place an atom inside allows to create a system where the atom is coupled to the vaccuumfield generating a stable system [1]. This generates a strongly coupled system of exciting physical effects, but it also has some limitations, namely that is is very hard to implement.

At this moment we are potentially standing on the verge of renewed innovation. In the field of cavity QED very stable systems have been made, but these systems come at a cost. The generation of integrated micro cavities is a difficult and labor intensive process, while the process degrades the coherence of the quantum dot. This motivates us re-evaluate open cavities. Specifically the open cavities with an exceptionally small mode volume Open micro cavities are easier to produce and, thanks to advances in the production of high quality micro mirrors. The possibility to shrink down the modevolume to the micro level allows us to increase the Purcell factor. An atom in a cavity experiences emission, the emitted photon when reflected by the mirrors, is able to interact with the photon itself. This allows us to couple the spontaneous emission of any atom in the cavity to the

cavity modes, increasing the amount the atom decay rate by the Purcell factor (F_P)[3].

In this thesis we will focus on building a strong foundation for such an open microcavity. In chapter 2 we will discuss the theory for the stability and transmission of the plane concave Fabry-Perot cavity, and we evaluate the energy distribution of multiple stable modes and how to evaluate the overlap of an incoming beam with the cavity mode.
In chapter 3 we will discuss the setup used to measure different aspects of the cavity transmission and how we evaluate data. In chapter 4 the results of the easiest form of the setup are discussed. The setup with a collimated beam. These results are compared with theory for consistency. In chapter 5 we show an in depth analysis of the ability to improve the system by matching incoming beams to the cavity fundamental mode using lenses. A very effective method to strengthen cavity effects on the Gaussian mode of a cavity. After this the thesis will be discussed and an outlook will be reviewed.

Chapter 2

The basics of the Fabry-Perot interferometer

A cavity in its most basic sense is a pair of mirrors between which a photon can be captured for a period of time [4]. The Fabry-Perot Instrument has properties which allowed late nineteenth century physicists to distinguish between different wavelengths of light. In a Fabry-Perot system light is transmitted through a mirror and consequently reflected between the mirrors multiple times, effectively bouncing around. Light entering the system obtains a repeating reflection pattern for specific cavity parameters. This is when light after a certain number of reflections regains its initial state, making a roundtrip. When such a roundtrip is made the light is able to interfere with itself. It can be so that the light accumulates a π phase difference such that the light destructively interferes after a roundtrip reducing the transmission through the system. Alternatively when a 2π phase is accumulated after a roundtrip the light will constructively interfere with itself which will result in maximal transmission. In this chapter we will discuss the stable transmission patterns or modes [5].

2.1 Basic properties of the Fabry-Perot Cavity

Let us consider a simplified example of a one dimensional Fabry-Perot. This can be seen as a pair of perfectly flat mirrors set up parallel to each other separated by a distance d, with a beam of light entering the system perpendicular to the mirrors. The light is partially reflected and partially transmitted, a process which is repeated at the second mirror.
This results in a transmission coefficient which adds the contribution of

the beam which is transmitted by the first mirror and transmitted by the second mirror after an arbitrary number of internal reflections:

$$T^{tot} = |t_1(1 + r_1 r_2 e^{i\frac{2\pi}{\lambda}d} + (r_1 r_2 e^{i\frac{2\pi}{\lambda}d})^2 + (r_1 r_2 e^{i\frac{2\pi}{\lambda}d})^3 + ...)t_2|^2,$$

where $t_{1,2}$ and $r_{1,2}$ are the transmission and reflection coefficients of mirror 1 and 2 and the exponentials describe the accumulated phase for a beam with wavelength λ after a $2d$ propagation. Adding the incoming wave and all contributions of reflections, and using the geometric series to simplify the series of contributions, we obtain a total transmission of:

$$T^{tot} = \frac{T^{max}}{1 + F\sin^2(\frac{\Phi}{2})}, \tag{2.1}$$

Here T^{max} is the maximum transmission scalar, for the lossless case this is equal to one. F is the coefficient finesse:

$$F = \frac{4R}{(1-R)^2},$$

The finesse dictates the sharpness of transmission peaks. Here R is the ratio of light which is reflected by the mirrors assuming equally reflecting mirrors. The coefficient of finesse is defined as the ratio of the distance between peaks and the width of those peaks. The presented finesse equation assumes lossless mirrors. A large coefficient of finesse contributes to a high quality cavity [5].
In **??** the parameter Φ is the accumulated phase within a roundtrip.

$$\Phi = \frac{4\pi d}{\lambda},$$

From the phase accumulation we can find the last important parameter of the Fabry-Perot, the Free Spectral Range (FSR). A cavity mode does not have a single constructively interfering solution but rather a set of evenly spaced transmission peaks separated by a frequency coinciding with a 2π phase accumulation in the mode. The FSR is defined as the frequency spacing of the transmission peaks, or the frequency shift needed to tune the cavity to the next transmission peak. The FSR can be defined as a frequency shift or a change in wavelength:

$$\lambda_{FSR} = \frac{\lambda^2}{2d} \qquad\qquad \nu_{FSR} = \frac{c}{2d},$$

The FSR assumes a fixed mirror separation. Changing the mirror separation changes the modes. Changing the mirror separation also results in a periodic transmission curve similar to the curve obtained when changing the frequency. Often the laser wavelength is adjusted to change the FSR instead of adjusting the mirror separation when tuning the cavity as modulating a laser on the nanometer scale is, in our setup, much easier then tuning a physical setup of two mirrors on the nanometer scale.
In Figure 2.1 we show a simulation of the transmission as a function of wavelength, for a cavity with a finesse of 155. The FSR and FWHM have been labelled.

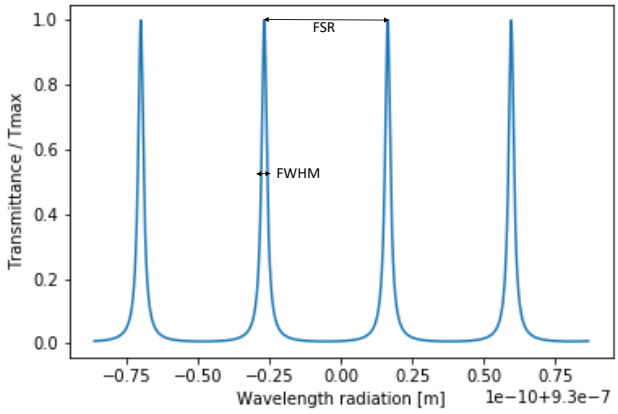

Figure 2.1: *Simulation of the transmission ratio of the cavity as a function of wavelength for a cavity with a finesse of 155. The transmission ratio is the transmitted light over the maximum transmitted light. The distance between the peaks is labelled as the Free Spectral Range (FSR) and the Full Width Half Maximum (FWHM) is labelled as well.*

Fabry-Perot with rays and the stability criterion

Light in a Fabry-Perot can be thought of in two ways. Light waves describes as a beam or light waves described as a ray. Beams consider the diffraction of light at large distances and phase shifts which represents physical light better then rays. Because of this we will use the beam representation when analysing obtained data in this thesis, however to obtain a basic understanding of a cavity we will shortly discuss resonance effects with rays. A ray is an idealized model of light. It is non divergent, and

is perpendicular to the wavefront of the light it describes [6]. Rays simplify the Fabry-Perot considerably making them ideal for discussing the stability criterion.
Cavities are build to trap light. Initially, it is easy to think of two parallel plane mirrors with a perpendicular ray bouncing back and forward between the two, however this is physically impossible to create. The smallest deviation in incident angle is enough to make the system unstable. To create a stable cavity will use a cavity with a single plane mirror and a concave mirror. The general idea is that the ray gets redirected with every reflection on the curved mirror to counteract the wandering of the beam, for stable solutions this will generate a closed path for which after a certain number of reflections the system repeats itself. This creates a reflection pattern for which a few examples can be seen in figure 2.2. The propagation path of the beam can be approximated using ray transfer matrices [5]. In order to use ray transfer matrices we must assume the reflection angle on the mirrors to be small (paraxial approximation). We can trace the ray to model the reflection pattern inside a cavity. In figure 2.2 simulations for different mirror separations are shown with a cavity with R = 300 mm. This leads us to a restriction for the cavity. If the distance between the mirrors becomes too large the ray will wander off into infinity on the x-y plane, making the system unstable. We find the condition for which a cavity is stable to be [7]:

$$0 < 1 - \frac{d}{R} \leq 1,$$

where d is the distance between the mirrors and R the curvature of the curved mirror. From this we find that the cavity is stable if d $< R$. For the simulations in figure 2.2 we used raytracing. To do this we defined a position of the ray as its location transverse to propagation and its angle with the propagation axis. We can manipulate the ray using ray tracing matrices which allow us to either propagate, diffract or reflect the beam. The simulations in figure 2.2 has been made by injecting a ray 1 cm off-centre. Depending on the mirror separation we can see very different solutions in the number of reflections fore a round-trip. Later we will see the connection to the wave-optical character of the cavity modes. A correctly reproduced effect of this method is the change in the FSR's dependence on mirror separation (d). The 2d in this equation stands for the propagation distance of the ray, when the ray reflects more often traversing the cavity one additional time for every reflection, the FSR becomes a multiple of the basic FSR. This highlights the importance of directing a light source on centre on the cavity.

Version of October 30, 2019– Created October 30, 2019 - 14:03

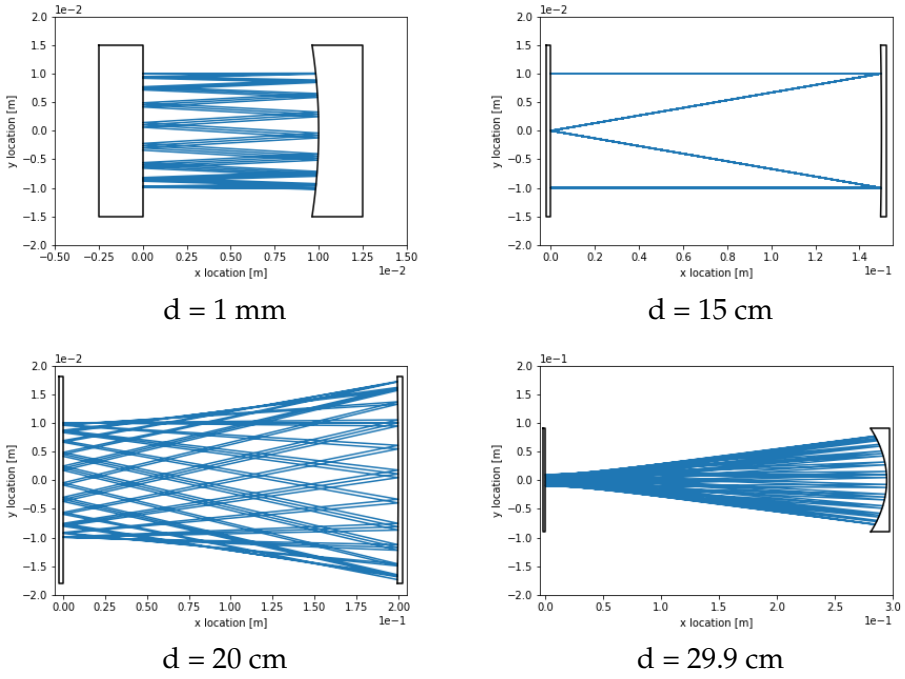

Figure 2.2: *Simulations of a cavity with a plane and curved mirror for several mirror distances. In each case the curved mirror has a curvature of 300 mm. The ray enters the system perpendicular to the plane mirror 1 cm above the midpoint. The ray has been modelled using ABCD matrices. The curvature of the mirrors is less visible in the d = 15 cm and d = 20 cm case due to scale, the d = 2.99 cm mirrors are drawn 5 times as big to compensate for diffraction.*

2.2 Fabry-Perot with beams and Transverse cavity modes

Fabry-Perot with rays provides a nice toy model for visualizing the effects of mirror curvature and stability. In order to build a working cavity in the lab we should advance to a model for light which represents a physical system, light as a beam. Beams have several effects that need to be taken into account when characterizing a cavity, which are not present in ray optics. Examples are the diffraction of light, the Gouy phase shift, and the focussing of a beam. In the next section we'll provide a compact explanation of the stable cavity modes which resonate with the beam, and discuss the properties of the fundamental mode. The fundamental mode, or the Gaussian mode, is the lowest order solution of the wave equation inside a cavity. It is the most common form of beam as it is the most useful for

cavity effects and is the easiest to work with. The fundamental mode has a Gaussian energy distribution in the transverse plane. The width of this Gaussian will either converge or diverge as the beam propagates toward or away from the focus. See the following equation for an exact description of the mode:

$$E(\rho,z) = E_0 \frac{\omega_0}{w(z)} e^{-\frac{\rho^2}{w^2(z)}} e^{-ikz + i\frac{k\rho^2}{2R(z)} - i\tan^{-1}(\frac{z}{z_0})},$$

Here ρ is the distance to propagation axis (z axis), k is the wavenumber of the light, w_0 is the beam waist which is defined at $z = 0$. This point is defined to be the focus of the beam. R(z) and w(z) are the wavefront curvature and beam width respectively at location z. Lastly, z_0 is the Rayleigh range, or the position for which $w(z_0) = \sqrt{2}w_0$. This is often seen as the location from where the divergence of the beam becomes notable and it is a useful constant to work with for any collimated beam.
We can describe all quantities in the Gaussian mode as a function of the Rayleigh range and position. Doing so results in the following equations:

$$w(z) = \omega_0\sqrt{1 + \frac{z^2}{z_0^2}} \qquad R(z) = z + \frac{z_0^2}{z} \qquad z_0 = \frac{k\omega_0^2}{2},$$

We show a visual representation of a Gaussian beam and its parameters in figure 2.3. The diffraction of the beam is clearly visible. A peculiar effect shows up when looking at high values of z. When we measure far enough away from the focus, when $z >> z_0$, we find that the width of the beam grows like $w(z) \propto z$. From the definition of the Rayleigh range it follows that the beam waist shrinks as the Rayleigh range becomes smaller. These effects tell us that small Rayleigh ranges allow for very strong focussing, but have the drawback of letting the beam diverge very fast.

The fundamental mode can be modelled to a physical cavity by fitting the curvature of the Gaussian function to the curvature of the mirrors. At the beam waist the curvature of the wavefront is zero: $R(z = 0) = 0$. Thus, we define the waist of the beam at the flat mirror. The radius of the fundamental cavity modes' wavefront at $z = d$ we define as the curved mirror radius (R): $R(d) = R$. Using the previously found parameters we can find the Rayleigh range of our cavity:

$$z_0 = \sqrt{d(R(d) - d)} = \sqrt{d(R - d)},$$

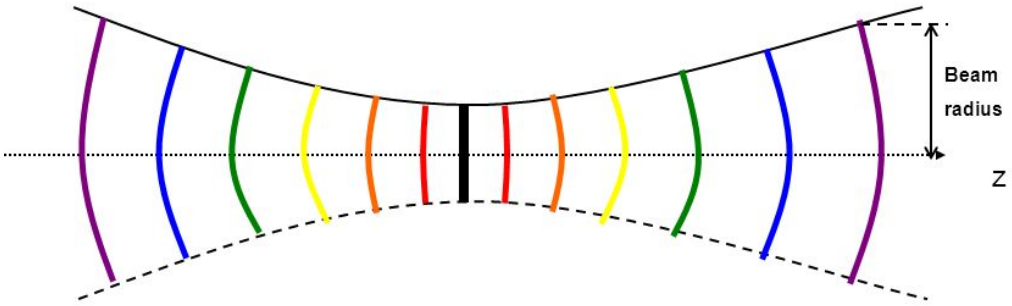

Figure 2.3: *A visual representation of a Gaussian beam. The black lines show the outline of the beam with the narrowest part at z=0. As $\|z\|$ grows the beam broadens. When z is large enough this will happen linearly with z. The curved lines represent the growing wavefront radius at larger z. Colors indicate a growing beam curvature as the distance from the waist grows.*

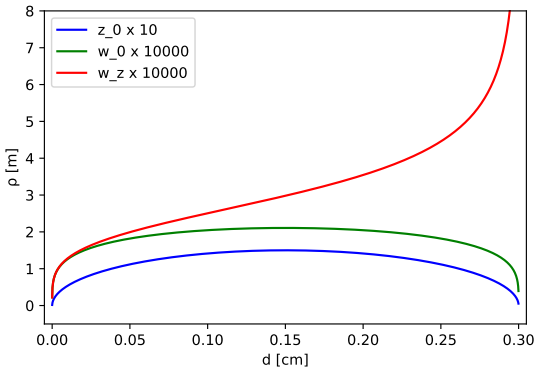

Figure 2.4: *A model of the cavity parameters' width as a function of mirror separation. Blue line: The Rayleigh range. Green line: Beam waist. Red line: Beam width at z = d.*

As we have discussed, all parameters for the fundamental mode can be modelled using the Rayleigh range and the distance to the focus. With the equalities given we can calculate the curvature of the beam wavefront and the beam width for any location, regardless of mirror separation or curvature of the curved mirror, assuming a stable resonator. Using these properties we are able to predict the behaviour of the cavity for any potential setup regardless of its scale. Figure 2.4 shows the results for a cavity with curved mirror radius R = 300 mm, over mirror separations from zero to the stability limit: $d = R$. We evaluate the Rayleigh range for this system, the beam waist, and the beam width of the beam at the curved mirror ($z = d$), for a beam with a wavelength of 950 nm.

2.3 Higher order modes

The Gaussian mode is the lowest order stable solution for a cavity, but it is not the only possible solution. As is visible in figure 2.2, a multitude of reflection patterns can provide a stable solution for which a repeating roundtrip can be made, this is also the case for wider beams. The intensity pattern does not have to be Gaussian in these solutions. For example, for the Hermite-Gauss modes, commonly derived in Cartesian coordinates, the intensity pattern at the beam waist can be described as the product of two Hermite polynomials, one for each dimension transverse the propagation axis. This intensity pattern will propagate similarly to the fundamental mode, diffracting in the same way. For a propagating higher order Gaussian beam, we obtain an electric field distribution as follows:

$$E(x,y,z)_{m,n} = E_0 \frac{\omega_0}{w(z)} H_n(x) \frac{\sqrt{2}x}{w(z)} e^{-\frac{x^2}{w^2(z)}} H_m(y) \frac{\sqrt{2}y}{w(z)} e^{-\frac{y^2}{w^2(z)}} \times e^{-ikz} e^{i\frac{k(x^2+y^2)}{2R(z)}} e^{-i(1+n+m)tan^{-1}(\frac{z}{z_0})},$$

Where $H_n(z)$ is the n'th order Hermite polynomial:

$$H_n(x) = (-1)^n e^{x^2} \frac{d^n}{dx^n} e^{-x^2},$$

$H_m(z)$ is identical to $H_n(z)$ but corresponds to the HG mode in the y direction. This combination of Hermite polynomials with a Gaussian distribution produces the Hermite-Gaussian (HG) modes. Each HG mode has an order. A higher order means a higher complexity. The mode number is equal to the sum of the modes for the Hermite polynomials: N = n + m. Measuring the intensity pattern of the laser we obtain patterns as shown in figure 2.5. By inspection of the modes, it is clear that the mode order in a specific dimension is equal to the amount of nodes in the intensity pattern [4]. Similarly, we obtain a family of higher-order modes when looking for solutions of the wave equation in cylindrical coordinates: the Laguerre-Gauss modes [8].

$$E(\rho,\phi,z)_{l,p} = \frac{1}{w(z)} \sqrt{\frac{2p!}{\pi(|l|+p)}} (\frac{\sqrt{2}r}{w(z)})^{2+|l|} L_p^{|l|}(z) \times e^{\frac{-\rho^2}{w(z)^2}} e^{-ik\frac{\rho^2}{2R(z)}} e^{-i|l|\phi} e^{-i(1+2p+|l|)tan^{-1}(\frac{z}{z_0})}$$

$$L_p^{|l|}(z) = \frac{x^{|-l|}e^x}{n!} \frac{d^n}{dx^n}(e^{-x}x^{n+\alpha}),$$

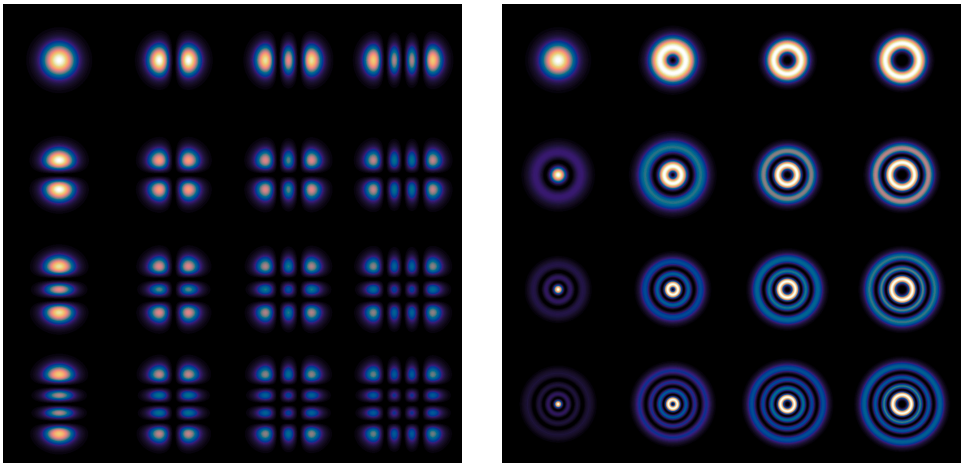

a) HG modes b) LG modes

Figure 2.5: *a) A family of Hermite-Gaussian modes. mode number m from 0 to 3 from left to right,*
mode number n from 0 to 3 from top to bottom b) A family of Laguerre-Gaussian modes. mode number l from 0 to 3 from left to right,
mode number ρ from 0 to 3 from top to bottom. Pictures from Guido Stam

Here we have indices ρ for the radial mode number, and l for the azimuthal part. $L_p^{|l|}$ is the Laguerre polynomial. When we plot different order modes we obtain the solutions shown in figure 2.5b. In contrast to the Hermite Gaussian modes we obtain the mode number for the Laguerre-Gaussian modes as N = 2p + |l|.

Theoretically LG modes describe systems with perfect rotational symmetry, however in practice obtained modes often are superpositions of multiple solutions[9]. Another option is a superposition of multiple LG modes. In systems with small astigmatisms in their rotational symmetry, the $\pm l$ can be distinct from each other. This degeneracy breaks symmetries between the two modes generating different field distributions which become superimposed with each other (figure 2.6). The superposition will generate a well defined axis for the lobes [10]. The generated pattern is called a cloverleaf pattern.

2.4 Coupling light into a cavity

We are able to improve the transmission of the cavity by coupling the light mode to the mode of the cavity. A Cavity will let through a very exact

Version of October 30, 2019– Created October 30, 2019 - 14:03

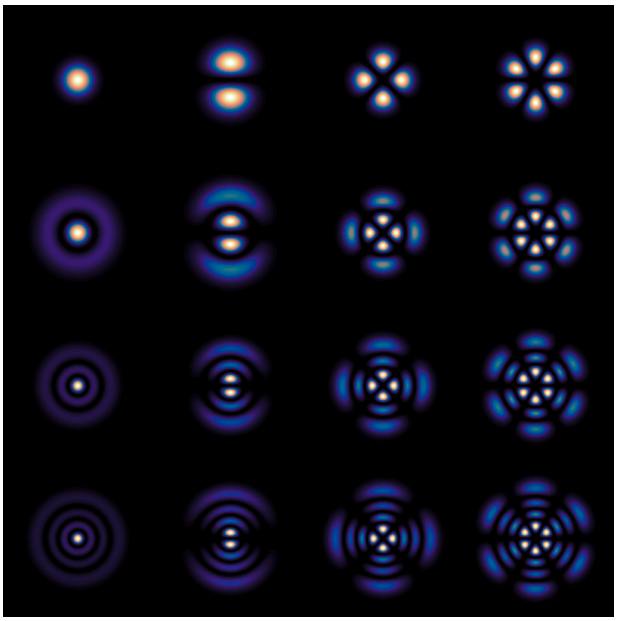

Figure 2.6: *A superposition of two LG modes. In certain systems the contributions of the l contributions to the LG mode do not equal those of the -l distributions. In these cases superpositions occur generating clover patterns.*

shape of light based on its parameters and filter all light which does not fit the cavity mode.
When coupling a source to a Gaussian cavity mode a Gaussian source is the most efficient. Examples of Gaussian sources are good lasers, or light coupled through a single mode fiber. The light beam will then need to have the same properties as the fundamental cavity mode, such as a beam width, location dependent curvature, and Rayleigh range. To maximize transmission through the cavity these parameters should be equal for the beam mode and the cavity mode at any point in space. Therefor the propagation axis of both modes should overlap, as should the curvature and width overlap at any point on that shared axis. This overlap can be quantified using the overlap integral [11]:

$$\eta = \frac{|\int E_1^*(z)E_2(z)dA|^2}{\int |E_1^*(z)E_1(z)|dA \int |E_2^*(z)E_2(z)|dA},$$

The overlap integral describes the overlap intensity of the Gaussian functions of the cavity ($E_1(x,y,z)$) and the beam ($E_2(x,y,z)$) in the x-y plane at a location on the z axis. The expression is normalized to be bounded between zero and one for no overlap and full overlap respectively. The

Version of October 30, 2019– Created October 30, 2019 - 14:03

outcome theoretically corresponds to the ratio of intensity which is transmitted through the cavity. This equation only holds for symmetrical and lossless cavities.

Chapter 3

The setup

3.1 Setup layout and equipment

We use a setup built around a half symmetric empty cavity. The cavity consist of 2 mirrors with 98% reflectivity for 950 nm light. We use a plane mirror and a mirror with a curvature of 300 mm. In figure 3.1 a schematical representation of the setup is shown. Vertical dimensions has not been taken into account in the figure as it does not have any effect on the measurements, but for completeness it is useful to note that the microscope objective is mounted at a height of 8 cm and the cavity is at a height of 10 cm.
The cavity is built on a tunable stage giving us the option to adjust the mirror distance between 1 mm and 15 mm giving us a large tuning range. We use two methods of observation behind the cavity. A photodiode is used to measure the transmission strength at points in a scan. It also allows us to lock the laser to a specific intensity. A beamprofiler is used to gain insight on the properties on a beam on different locations in the setup. To do this a lock is necessary thus the signal is split by a beamsplitter to be measured simultaneously. We have connected the laser output directly to a commercial Fabry-Perot interferometer (FPI). This is used to check if the laser remains stable through its scan range. The lens is added to match the modes of the incoming beam to that of the cavity. We will go into more detail on this later on. We collimate the light from the fiber with a microscope objective. The microscope objective is used as a very strong lens with a working distance of 1.2 mm. This allows us change the beam collimation properties with very little to no effect on the distances of the setup. Initially we have attempted to collimate the beam as much as possible and have succeeded in keeping the beam parallel (non convergent)

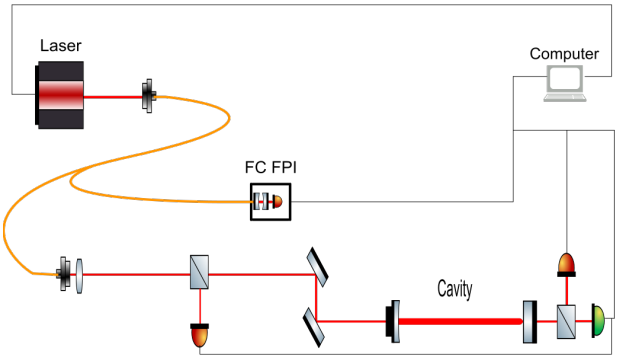

Figure 3.1: *Graphical representation of the setup. Red lines depict open laser beams, and yellow wires correspond to fiber coupled objects. Red detectors are photo-diodes and the green detector is the RayCi beamprofiler. Height differences between objects is ignored.*

for multiple meters.

In order to accurately measure the beamprofiles we use a Toptica lockbox. We do not use the full capabilities of the lockbox, what we use is a single PID controller capable of applying a feedback signal to the laser to account for mechanical drift in our system. Thermal noise is still present in the system.

The lockbox allows the system to account for small mirror fluctuations by tuning the lasers' wavelength to fit the altered cavity mode. Assuming a strong enough signal, when the mirrors drift, the peaks will shift, and by tuning the laser wavelength we can make sure the transmission intensity remains constant. We call this locking to a mode. Using this method we can lock to a mode for several minutes, as opposed to the seconds it takes to lose the mode without locking, allowing us to accurately measure the beamprofile using the RayCi CCD camera. We use the most straightforward method of locking, the side-of-fringe method. This method does not lock on the peak of a mode, but to a side of a peak. This makes locking easier as small deviations will generate large differences in the transmission and also makes the direction of drift visible. When locking to the top of the peak both drift directions make the cavity transmission smaller, making it hard to distinguish whether the cavity distance shrinks or grows. This caveat can be counteracted by using the Pound Dremer Hall method, which should still be implemented. The drawback of using the side of fringe method is that we have to work with lower transmission coefficients and need a higher finesse as overlap between modes becomes a larger issue. For our goals these issues are minor, and we have encountered no necessity for improvement as of the moment of writing.

3.2 The laser properties and limitations

We use a DL pro scannable laser with a mechanical range of 915 to 985 nm. The laser has been tuned to operate at a wavelength of 938 nm. Attached to the laser is a SC 110 from Toptica photonics which allows us to control the wavelength, by applying voltage to an internal piezo element to modify an internal grating in the laser. We use other Toptica modules allowing us to control the temperature and intensity, and a module that provides feedback such that we can lock the laser to the cavity.
Despite the laser being tunable over a 70nm range, this is larger then our effective scanrange. When scanning over a range of piezovoltages the laser mode can change affecting both the output wavelength and the output intensity unpredictably. To visualize this effect, and to calibrate our laser to a single mode, we place the photodetector in front of the cavity to measure the beam directly after collimation, and look at the signal of a commercial Fabry-Perot interferometer with a FSR of 4GHz see figure 3.1. In figure 3.2 the erratic behaviour of the laser is shown when tuned incorrectly.

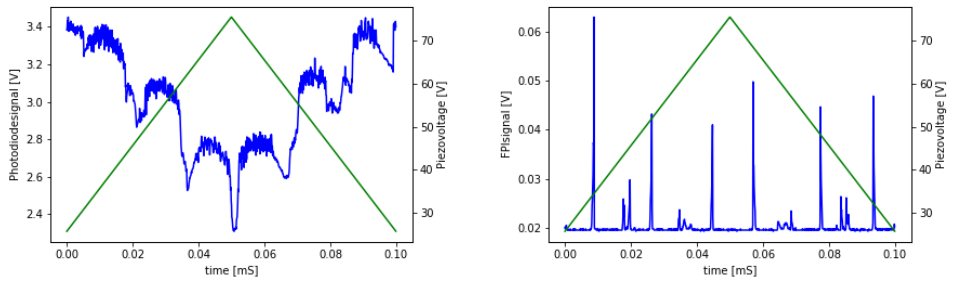

a) b)

Figure 3.2: *a) Blue line: The laser output before the cavity as a function of time. Erratic behaviour is caused by modejumps that need to be suppressed. Green line: Piezovoltage as a function of time. b) Blue line: The transmission of the fiber coupled Fabry-Perot over time. Equidistant peaks are expected when functioning on a single mode, the subpeaks indicate sudden a shift in frequency in the laser. Green line: Piezovoltage as a function of time.*

To surpress these signals we have applied a feedforward which manipulates the intensity of the laser to keep it to a single mode. The total output intensity was decreased to stabilize the lasermode, this results in the stable output as seen in figure 3.3

From these measurements we find that we can scan accurately between piezo voltages of 20V and 70V giving us quite a large scan range. From the

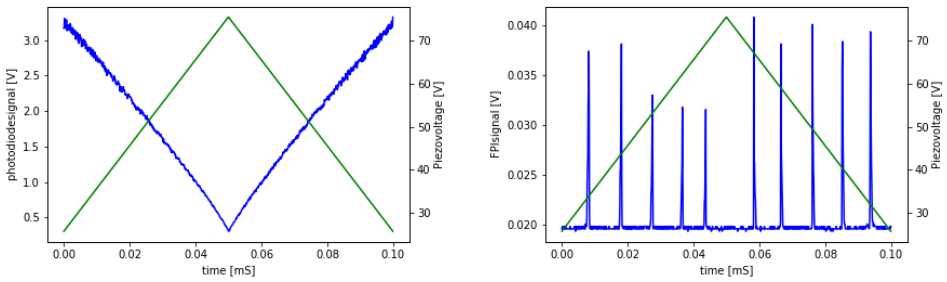

a) b)

Figure 3.3: *fig a) Blue line: The laser output before the cavity as a function of time. No modehops are detected Green line: Piezovoltage as a function of time. fig b) Blue line: The transmission of the fiber coupled Fabry-Perot over time. Equidistant peaks are obtained indicating the laser is scanning over a single mode for piezo voltages under 70V Green line: Piezovoltage as a function of time.*

Fabry-Perot measurement we find that between 32V and 67V the FPI has 4 peaks, with a FSR of 4 GHz for the FPI we find that a single volt corresponds to a 0.46 GHz frequency shift. This gives us a scanrange of 23 GHz.

In 3.3 we can see the laser intensity diminishing when the piezovoltage rises. This effect is suboptimal, however it is predictable and can be accounted for during measurements.

Chapter 4

The setup without lens

In this chapter we will be evaluating and discussing the measurement obtained when illuminating the cavity with a nearly collimated beam. A collimated beam does not allow for optimal matching of the modes between beam and cavity. In our set up we have measured a coupling efficiency of 0.075 for the fundamental mode. With this coupling we obtain a high enough signal to noise ratio to evaluate the transmission spectrum for LG modes. The advantage of using a collimated beam over a beam matched to the fundamental mode is that higher order modes are not suppressed, as coupling to a specific mode suppresses the other modes. This will allow us to more easily analyse the transmission spectrum within a free spectral range. To fully characterize the current setup we evaluate the signal of the four different inputs discussed in the previous chapter. The photodiode signal allow for the evaluation of the modes and the FSR through measuring the transmission spectrum through the cavity. The beampofiler will be used to evaluate the shape and size of various modes. The FPI and pre-cavity measurements will be used for quality control and normalization.

4.1 Analysing a Free Spectral Range

We verify the quality of the cavity by evaluating the transmission spectrum within a free spectral range and the ordering of the modes within it. We must make sure the cavity transmission is dominated by cavity modes of a high quality and not by direct transmission, or overlapping modes due to low finesse. We present the transmission of the cavity as a function of the tuning piezo element voltage in figure 4.1.
We have obtained a set of narrow peaks with nearly equally spaced. The

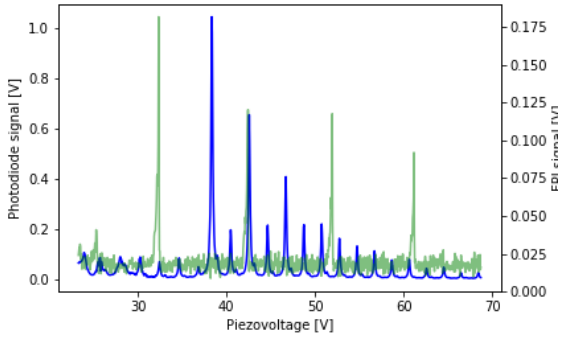

Figure 4.1: *Cavity transmission as a function of the piezovoltage.. The signal is the total intensity of the beam. blue curve: cavity signal. green curve: Fabry-Perot Interferometer (FPI) signal*

narrow peaks as opposed to the peak separation indicate a high quality cavity. Additionally we find a modehop-free laser input by noticing equally spaced transmission peaks of the FPI.. We further evaluate the spectrum by locking to prominent peaks to find the corresponding modes. We have locked onto the highest intensity peak and the 6 peaks to its right. The peak locations and corresponding modes are shown in figure 4.2. Checking with the theory for higher order modes we find that the modes to correspond the modes in the cloverleaf LG-modes discussed in chapter two. The modes have been labelled with their LG mode number. We find the mode ordering to coincide nicely with the predicted order as shown in table 4.1. The equal spacing of the cavity modes and the

N	0	1	2	3	4	5	6
ρ	0	0	1	1	2	2	3
l	0	1	0	1	0	1	0

Table 4.1: *$N = 2\rho + |l|$, ρ is the radial order, l is the azimuthal order*

agreement with the predicted mode ordering shows that the cavity operates well without dominating systematic errors [9]. We have searched for higher order modes for $l > 1$ but we have not been able to identify any of these modes. It is expected that these modes don't have a sufficient signal to noise ration to be detected. We conclude that we have found stable and predictable cavity modes using our system.

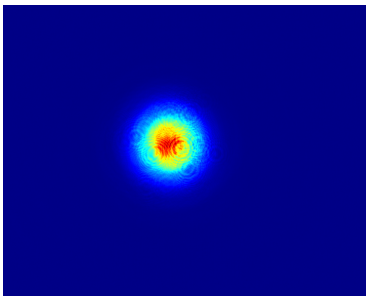

a) $\rho = 0, l = 0$

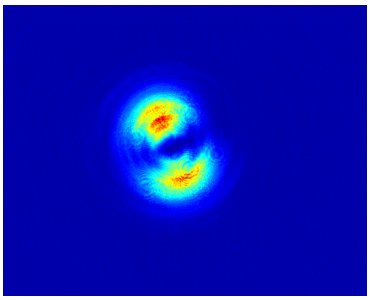

b) $\rho = 0, l = 1$

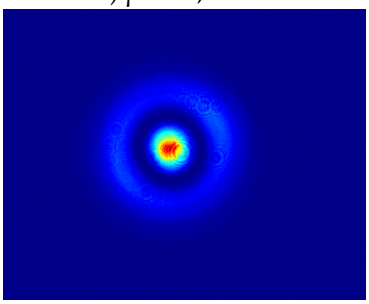

c) $\rho = 1, l = 0$

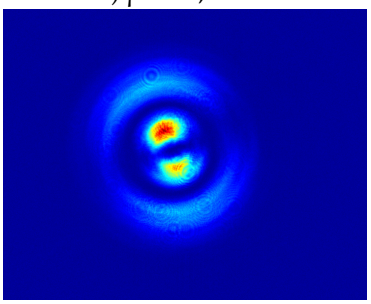

d) $\rho = 1, l = 1$

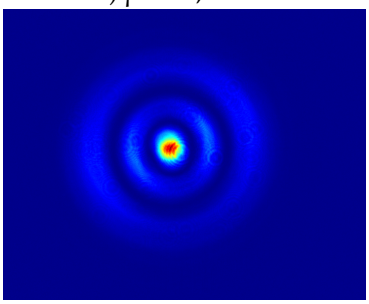

e) $\rho = 2, l = 0$

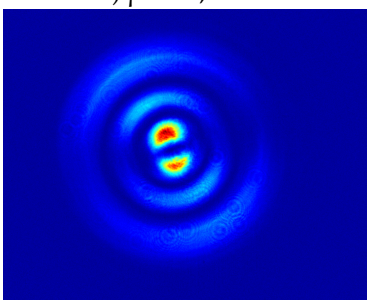

f) $\rho = 2, l = 1$

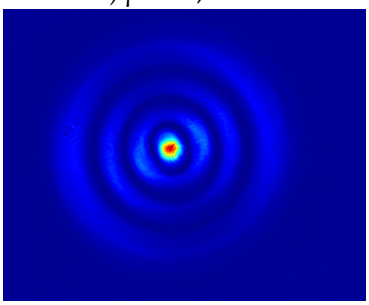

g) $\rho = 3, l = 0$

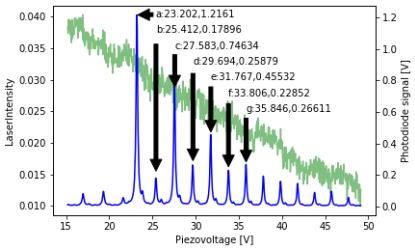

h) The transmission over laser frequency.

Figure 4.2: *a-g) show the beam profiles of different peaks in the cavity spectrum. The peaks are locked to the side of the intensity peak on the positive side. each mode has its $TEM_{\rho,l}$ denotation shown below it. h) shows the peaks locked onto. Arrows indicate the peak locations and refer to the modes. The peaks seem to nicely fit the $2\rho + |l|$ modes.*

4.2 Characterizing the cavity parameters

In this section we will evaluate the cavity parameters of our setup. We have used to mehods to determine the cavity mirror spacing. First we evaluated the FSR, and secondly we measured the beam properties of the fundamental mode behind the cavity. By comparing the two results and the estimated mirror separation we can deduce all relevant parameters.

4.2.1 Evaluating the Free Spectral Range

For the evaluation of the FSR of the system we obtain the data presented in figure 4.3. In these figures we show the transmission spectrum of the cavity over an estimated 1.5 FSR. This spectrum contains two fundamental modes. The mode strenght is largely effected by fluctuations in laser intensity as discussed in chapter 3. These peaks are separated by the physical FSR and can be used to find the exact value of the FSR in the frequency domain. To do this we compare the separation between the fundamental to the peak separation between the FPI peaks as the FPI is known to have a FSR of 4GHz. Inspection of the FPI peaks reveal the frequency detuning of the laser to be non linear as the piezo voltage is tuned. Figure 4.4 shows the dependence of the frequency detuning as a function of the piezo voltage. We have found a second order polynomial to fit the detuning nicely. After conversion the peak separation is consistent within 0.1GHz. Resulting in the graphs shown in figure 4.5, where we find the free spectral range to be 14.1 ± 0.1 GHz for both measurements.
Using the theory presented in chapter 2 we this corresponds to a mirror separation of 1.065 cm. This is in agreement with the measured mirror separation of 1 cm.

To solidify the conclusion of us having found the FSR we evaluate the diminishing peak intensity we normalize the transmission strength with the intensity of the laser. This is done solely for the second measurement as the laser intensity nears zero for the first measurement generating instabilities in the laser intensity around the low intensity fundamental mode, and corresponding higher order modes as is visible in the presented figures by the missing higher order modes. Figure 4.6 shows the normalization of the second measurement which has generated a nearly perfectly repeating transmission profile at a detuning of 14.1 GHz. Small fluctuations are still present due to high frequency laser fluctuations, and thermal fluctuations.

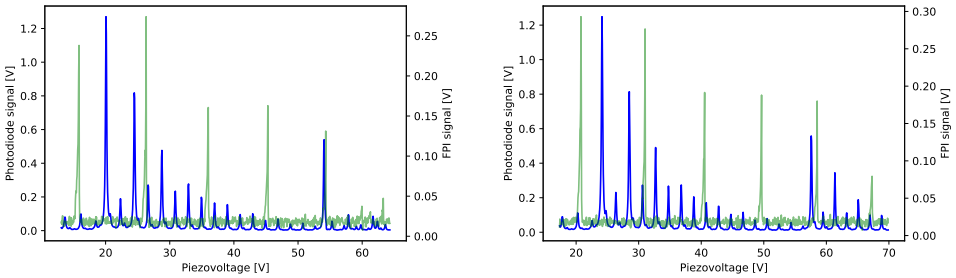

Figure 4.3: *Two measurements of the cavity transmission spectrum. The blue curves show the transmission spectrum of the cavity over more then a FSR, showing two fundamental modes. The green curves show the transmission of the FPI. The distance between the FPI peaks is 4 GHz.*

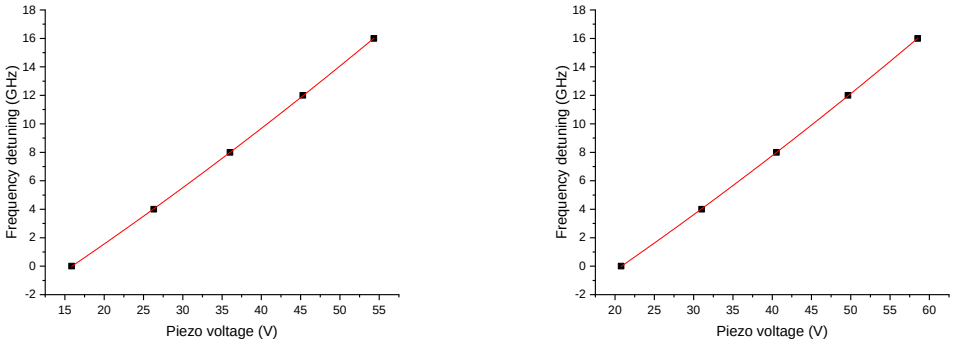

$\Delta\nu = 0.001U^2 + 0.34U - 5.7$ $\Delta\nu = 0.001U^2 + 0.34U - 7.5$

Figure 4.4: *Models of the frequency detuning as a function of the piezo voltage for two measurements. The black points correspond to piezo voltages where FPI peaks are found as a function of detuning from the first peak for each measurement and the second order polynomial fit is shown with the red line. The second order polynomial fit is used to convert the piezo voltage to the frequency ($\Delta\nu$) detuning from the left most FPI peak.*

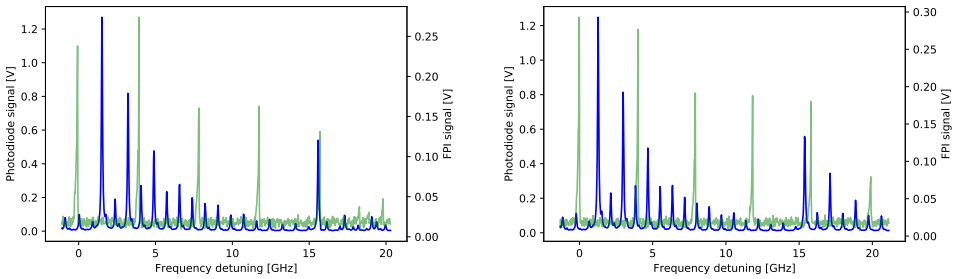

First measurement Second measurement

Figure 4.5: *Two measurements of the cavity transmission spectrum (blue curve) and the external FPI spectrum (green curve). The blue curve shows one full transmission spectrum for the cavity, and a second first order mode between 50 and 60 Volt for the piezo in both measurements. Intensity differences are caused by diminishing laser intensity as the piezo voltage rises (figure 4.6). The distance between the FPI peaks is 4 GHz.*

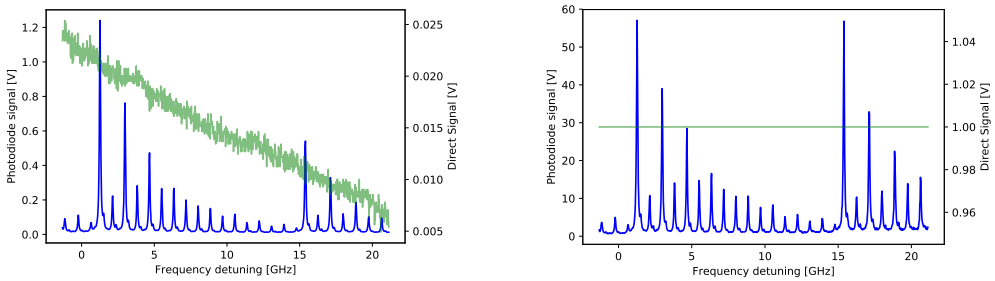

Non-normalized Transmission spectrum normalized Transmission spectrum

Figure 4.6: *a) Green curve: The laser intensity before the cavity. Blue curve: The transmission spectrum of the cavity. b) Green curve: Normalized direct measurement. Blue curve: The transmission spectrum of the cavity after normalizing with the laser intensity. Peak intensities in the transmission equalize confirming that we have found FSR. Small deviations in the two transmission spectra are due to laser fluctuation and mirror vibrations.*

4.2.2 Evaluating the fundamental mode

The second method we use to check mirror separation and subsequently the mirror curvature is by the evaluation of the beam width of the fundamental mode after the cavity. Using the Gaussian beam parameters (chapter 2) we find the mirror separation to be deducible after fitting the wave front curvature to the curved mirror curvature.
Using the beamprofiler we obtain a 2D intensity pattern of the Gaussian beam as shown in figure 4.7. The intensity pattern, as a function of the Gaussian beam parameters, is given as:

$$I = E_0^2 \frac{w_0^2}{w^2(z)} e^{\frac{-2\rho^2}{w^2(z)}} = I_{max}(z) e^{\frac{-2\rho^2}{w^2(z)}}$$

From here it is easy to deduce the that, from the intensity pattern, the beam radius is determined where the intensity e^{-2} of the maximum intensity. Figure 4.7b shows the x cross-section of the 2D heatmap with the e^{-2} width visualized.

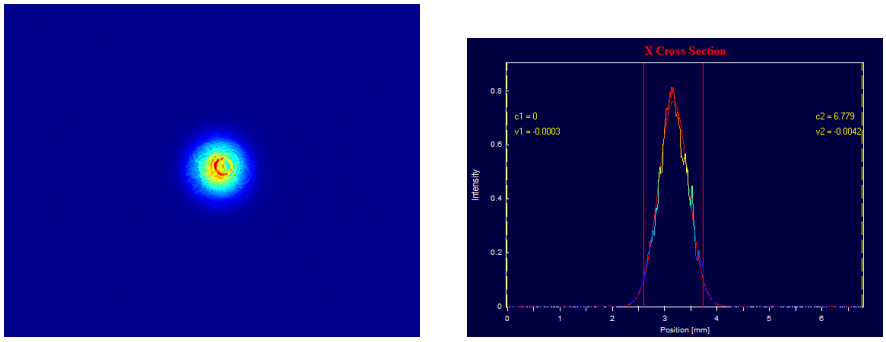

a) Heatmap b) x cross-section with beam width

Figure 4.7: *a) The beam profiler signal. It is a 2D heat map which logs the intensity on a area. The exposure time we used in general and for this figure is 700µs. A Gaussian distribution is shown. b) Cross section of figure a with the e^{-2} width visualized.*

We have evaluated the width of the beam at three different locations twice and plotted the expected Gaussian width of d = 1.065 over the these points (figure 4.8). To fit the expected cavity mirror separation we assume the measurement locations to be in the far field regime as this allows us to assume the beam width to grow linearly with the measurement distance. This results in a fitted mirror separation of 1.16 cm which is also represented in figure 4.9. The fit is not perfectly coinciding with the measured

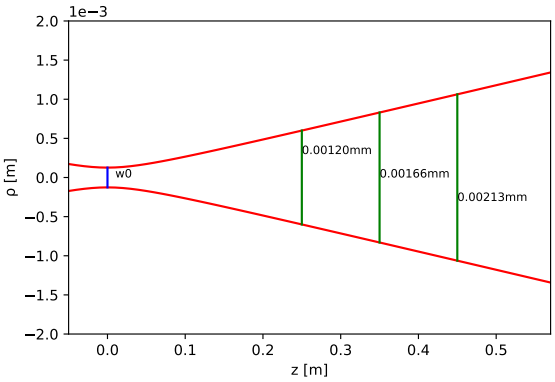

Figure 4.8: *A simulation of the the Gaussian mode for our setup. R = 300mm, d = 1.065cm. At z = 0.25 cm, z = 0.35 cm and z = 0.45 cm we included a green line and its length representing the beam width (W(z) = $\frac{I_{peak}}{e^2}$) at the specified z.*

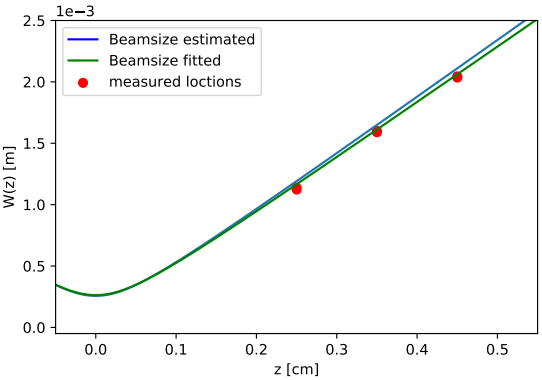

Figure 4.9: *Blue line) represents the Beam width as calculated in figure 4.8. Red dots) represent 6 measurements behind the cavity, Green line) The fit through the measurements. We found the mirror distance to be 1.16 cm.*

points, which is due to the fact that we are not fully in the far field regime. This is considerably larger then the previously estimated measurements, but we have some potential errors in the system. In the setup we have measurement errors on beamprofiler location, and we have not taken the light propagation in the mirror or beam splitter into account resulting in beam deformation Beside this we have found elliptical beam profiles instead of perfectly circular profiles. This is expected to be caused by a rotation of the beamprofiler. This elongates one of the axis. With the errors we find that the estimated mirror separation of 1.2 cm this is within the same order of magnitude but should be improved.

Chapter 5

Improving the setup through modematching

Having successfully created a tunable cavity we are presented with the challenge to improve on it. We have generated a model to do so through mode matching. Coupling the fiber mode to the cavity mode. This can be done using lenses to match the mode of the incident beam to the cavity mode.

To model the coupling efficiency we make use of the complex beam parameter. This is a single element q containing all Gaussian parameters:

$$q = z + iz_r \qquad \frac{1}{q} = \frac{1}{R(z)} - i\frac{\lambda}{\pi w^2(z)}$$

The complex beam parameter provides the advantage of using ray transfer matrices when describing the propagation and diffraction of a beam. Ray transfer matrices are traditionally used for describing rays [5]. The matrices will also work for the complex beam parameter when used in the following way:

$$\begin{pmatrix} A & B \\ C & D \end{pmatrix} q = \begin{pmatrix} A & B \\ C & D \end{pmatrix} \begin{pmatrix} q \\ 1 \end{pmatrix} = \frac{Aq + B}{Cq + D}$$
$$\begin{pmatrix} A & B \\ C & D \end{pmatrix} \frac{1}{q} = \begin{pmatrix} A & B \\ C & D \end{pmatrix} \begin{pmatrix} 1 \\ \frac{1}{q} \end{pmatrix} = \frac{A + \frac{B}{q}}{C + \frac{D}{q}}$$

Here a matrix with components ABCD correspond to a matrix describing propagation or diffraction. With specific transfer matrices we can use linear algebra to describe the beam at any location z, taking the effects of any and all optical elements in its path.

The important matrices we use are the propagation matrix and the matrix of an ideal lens with focal length f:

$$\begin{pmatrix} 1 & \Delta z \\ 0 & 1 \end{pmatrix} q(z) = \frac{q(z) + \Delta z}{0 + 1} = q(z + \Delta z)$$
$$\begin{pmatrix} 1 & 0 \\ \frac{1}{f} & 1 \end{pmatrix} \frac{1}{q(z)} = \frac{1}{q(z)} - \frac{1}{f}$$

Here we have also shown the validity of use of ray transfer matrices as the results coincide with the expected results for the rays as shown in [5].
Using these basic elements we can build a multi variable simulation of modes for the beam and cavity respectively and compute the mode overlap at any location. We make a simulation with a microscope objective and a regular lens as optical elements as seen in figure 5.1. We present the 4 distances z_i which we can control, for our purpose we have set z_{tot} to coincide with the current lab setup. Because of this we also fix z_{obj} to be equal to the working distance of the microscope objective to collimate the beam as effectively as possible.

We find the Rayleigh ranges of the modes using the standard formulas:

$$z_{r,cavity} = \sqrt{d(R-d)} \qquad z_{r,fiber} = \frac{\lambda}{\pi NA^2}$$

Here the NA is the Numerical Aperature of the single mode fiber. The fiber we use has an NA of 0.13. Combining every discussed part we can simulate the overlap of the modes at location z_{loc} for which we will take the location of the curved mirror as value as it is the most relevant location to have a high coupling.

In terms of ray transfer matrices the propagation and diffraction looks as

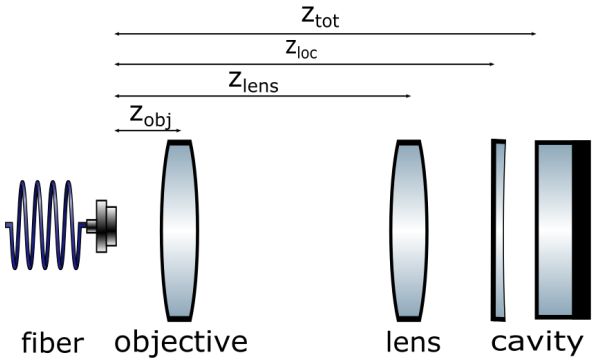

Figure 5.1: *Visualization of the lenses in the simulation. Multiple variable distances have been labelled.*

followes:

$$q'_{fiber} = \begin{pmatrix} 1 & (z_{tot} - z_{lens}) \\ 0 & 1 \end{pmatrix} \begin{pmatrix} 1 & 0 \\ \frac{-1}{f_{lens}} & 1 \end{pmatrix} \begin{pmatrix} 1 & (z_{lens} - z_{obj}) \\ 0 & 1 \end{pmatrix} \begin{pmatrix} 1 & 0 \\ \frac{-1}{f_{obj}} & 1 \end{pmatrix} \begin{pmatrix} 1 & z_{obj} \\ 0 & 1 \end{pmatrix} q_{fiber}$$

$$q'_{cavity} = \begin{pmatrix} 1 & -(z_{tot} - z_{loc}) \\ 0 & 1 \end{pmatrix} q_{cavity}$$

Here I have set up an independent complex beam parameter for both modes, q'_i indicates the value for q at z_{loc} for each beam respectively. The negative propagation direction used in the matrix working on q_{cavity} is because the cavity mode propagates in the opposite direction of the fiber mode Note that we have assumed the objective to function as a thin lens, this is not a perfect assumption but is accurate enough for our purposes.

With the q's for both modes known at the same location we can set up the normalized overlap integral presented in chapter 2. We formulate the Gaussian energy distribution as a function of q and label it u, after which we compute the integral and end up with the coupling effeciency as a function of $\lambda, R_1, R_2, w_1, w_2$ where R_i and w_i are the wavefront curvatures and mode widths at z_{loc} for the fiber mode and cavity mode respectively.

$$\eta = \frac{|\int u_1^* u_2 dA|^2}{\int |u_1^* u_1| dA \int |u_2^* u_2| dA} \qquad u_i(z) = \frac{1}{q_i} e^{\frac{-ikr^2}{2q_i(z)}}$$

$$\eta = \frac{(2\lambda R_1 R_2 w_1 w_2)^2}{(\pi w_1^2 (R_1 - R_2))^2 + (\lambda R_1 R_2 (w_1^2 + w_2^2))^2} \qquad 0 \geq \eta \geq 1$$

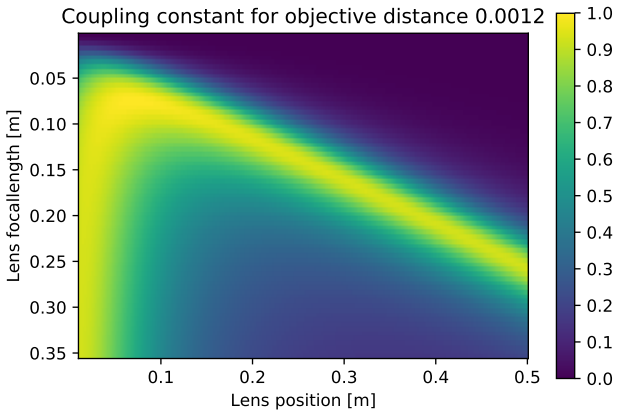

Figure 5.2: *Simulation of the coupling efficiency for lens strength f and postion z_{lens} for a microscope objective placed at the working distance.*

We compute q'_{fiber} for lenses with focal lengths between 1 cm and 35cm at positions from 1 to 50 cm to the plane cavity mirror. The results are presented in figure 5.2. when solving the coupling efficiency integral we obtain coupling efficiencies up to .999 given a lens with a focal length of 7.1 cm at a distance of 6.9 cm. We obtain a small difference in the the focal length and the optimal lens position. This is due to the propagation between the objective and the lens. When we use a perfectly collimated beam the optimal position of the lens would be at the focal point, however the beam diverges slightly between the optical elements. The small displacement compensates for this effect. The simulation seems to be working nicely and can be altered to fit any system as of now. The high coupling at low lens positions is not completely understood. This regime is not accounted for in the system as it does not describe a physically relevant regime where the lens is placed inside the cavity.

Chapter 6

Outlook and conclusion

Over the course of the previous few months we have been able to lay the groundwork of the production of the desired micro cavity. We have created a concise evaluation of the theory for the macroscopic Fabry Perot interferometer and build a system which shows the properties of a high quality cavity. Using a commercial Fabry Perot and measurements we have calibrated the light source and used this to determine the mirror separation of the cavity using two different methods, and found this to be consistent with theory and estimation. We have found both measurements to be consistent with estimations during the building of the cavity and with each other verifying the correctness of our theory. Also a simulation has been build to optimize the coupling of the modes in order to most efficiently couple the fundamental cavity mode to incoming light. This characterization has been a success and provides a base for future research. A possible continuation is the characterization of the coupling efficiency to compare to the modelled results. A well coupled beam should drastically improve the throughput of the cavity. Other mechanical improvements can still be made to the system which can improve on discussed system caveats. After this the system is ready to implement the micro mirrors, after which all characterization can be repeated.

Bibliography

[1] Andreas Reiserer and Gerhard Rempe. Cavity-based quantum networks with single atoms and optical photons. *Reviews of Modern Physics*, 87(4):1379–1418, December 2015.

[2] T. Steinmetz, Y. Colombe, D. Hunger, T. W. Hansch, A. Balocchi, R. J. Warburton, and J. Reichel. Stable fiber-based Fabry-PÃ©rot cavity. *Applied Physics Letters*, 89(11):111110, September 2006.

[3] E. M. Purcell. Theory of long period magnetic relaxation. *Phys. Rev.*, 69:681, Jun 1946.

[4] J. M Vaughan. *The Fabry-Perot interferometer.* Hilger, 1989. OCLC: 60018035.

[5] Justin Peatros and Michael Ware. *physics of light and optics*. 2015 edition, March 2016.

[6] Robert R. Shannon. *The Art and Science of Optical Design*. Cambridge University Press, 1 edition edition, June 1997.

[7] L Casperson. Mode stability of lasers and periodic optical systems. *IEEE Journal of Quantum Electronics*, 10(9):629–634, 1974.

[8] Syed H Murshid. *Optical Fiber Multiplexing and Emerging Techniques: SDM and OAM*. IOP Publishing, 2019.

[9] Francesco Pampaloni and JÃ¶rg Enderlein. Gaussian, Hermite-Gaussian, and Laguerre-Gaussian beams: A primer. page 29.

[10] Darryl Naidoo, Andrew Forbes, Kamel Ait-Ameur, and Marc Brunel. Constructing petal modes from the coherent superposition of Laguerre-Gaussian modes. 7913:791304, February 2011.

[11] Kevin J Garcia. Calculating component coupling coefficients. *Laser focus world*, 36(8; SUPP/1):51–56, 2000.

Version of October 30, 2019– Created October 30, 2019 - 14:03